Article

Poromechanical Modeling and Numerical Simulation of Hydraulic Fracture Propagation

Xinsheng Zhang, Yunxing Cao, Li Wang,* and Guo Xiaohui

Read Online

ACCESS | Metrics & More | Article Recommendations

ABSTRACT: Hydraulic fracturing (HF) is an important technique for enhancing the permeability of petroleum and gas reservoirs. To understand the coupling response mechanism of fluid pressure and in situ stress during the expansion of hydraulic fractures— based on the theory of the fluid flow of seepage porous media and damage mechanics—a poromechanical model of hydraulic fracture propagation is proposed and the finite element method (FEM) numerical weak coupling calculation method of hydraulic fracturing is realized. First, the effect of the coupling stress field is described by introducing the β value of the amount of pore volume that varies, resulting from internal pressure per unit of fluid internal, and the coupling calculation method of the pore pressure-effective stress-element damage-pore pressure expansion coefficient is formulated. Second, based on the concept of damage localization, a calculation method for the hydraulic fracture opening equation is proposed, and then the element damage-hydraulic fracture opening-permeability tensor-pore pressure field calculation cycle is established. The model indicates four stages of fracture propagation: I, fracture nucleation, II, kinetic propagation, III, steady propagation, and IV, propagation termination. Finally, as an example, a numerical simulation of three-dimension hydraulic fracturing is performed. In comparison to previous research, the morphology of the fracture zone and the fluid pressure contour of the horizontal section are approximately ellipses, which verify the feasibility of the weak coupling calculation method; the fracture parameters verify its accuracy, which include the length, width, and fluid pressure.
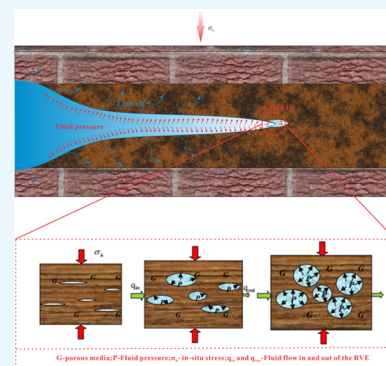
1. INTRODUCTION

Hydraulic fracturing (HF) is an important technique to enhance the permeability of petroleum and gas reservoirs. The mechanisms of fracture propagation are explained well by analytical solutions (2D,[1−3] P3D,[4,5] and PL3D[6,7]), which mainly deal with the lubricant flow, elastic displacement of fracture walls, and incomplete coupling between the fluid front and the fracture tip. However, the analytical solutions can only output the temporal and spatial distributions of hydraulic fracture parameters such as fracture opening, length, and fluid pressure on a predefined propagation path. Even some finite element methods (FEMs),[8−11] based on cohesive zone models, need to predefine the propagation path on a lined node. These models essentially place the parallel plate crack model in an infinite elastic body. Although they have good planar applications, the complexity of grid technology is a disadvantage factor for large-scale engineering applications. And they ignore the temporal and spatial distributions of stress, damage, and pore fluid pressure around the injection hole, which are significant for monitoring the hydraulic fracture zone growth and assessment of permeability enhancement.[12,13]

In addition, some microscopic models are also used for the numerical simulation of hydraulic fracturing, such as discrete element models (DEMs),[14,15] discrete fracture seam network model (DFN),[16,17] and lattice model (Lattices).[18,19] These

models mainly reflect the microscopic formation of crack mechanism, focusing on the complexity and microseismic properties of cracks. This method has a certain arbitrariness in determining the microscopic primitive mechanism and attribute parameters. It will lead to fluctuations in the macroattribute evaluation, which is not conducive to large-scale engineering applications and evaluation.

The poromechanical model can satisfy both the needs of assessment of hydraulic fracture propagation. It is based on the coupling analysis between the porous flow and stress and damage utilizing the FEM, which comprises direct coupling and load transfer methods.[20] The former is also referred to as strongly coupled, where the final solutions of the unknown multiple physical field variables are recovered by solving the simultaneous equations. However, many engineering problems do not satisfy the conditions of strong coupling, especially for some dynamical evolution problems such as damage-induced
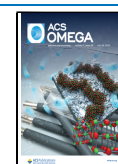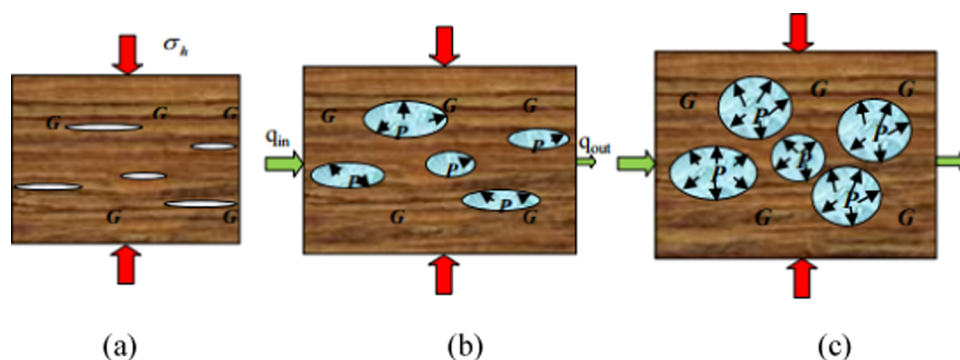
Figure 1. Porosity–elastic coupling conceptual model: (a) the initial stage, (b) pressure gradient gradually increasing stage, and (c) the steady-flow stage. G: porous media; P: pore fluid pressure; σ_h: in situ stress; and q_{in} and q_{out}: fluid flow in and out of the RVE, respectively.

fracture, where it is difficult to ensure solution convergence. The load transfer method approaches a solution of the unknown field variables by successively solving the multi-physical field equations, where one field variable is used as an input for the solution of another, which is repeated through a sequence of couplings until a tolerance for an equilibrium solution is reached. This load transfer, sequential, or leap-frog method represents only weak coupling and since fluid-driven fractures are always evolving; therefore, this method is particularly appropriate for dealing with the nonlinearities in these problems. However, there are some key points in the poromechanical model to be dealt with, such as how to define the fracture opening using the continuum variables, how to deal with the strain energy loss resulting from hydraulic fracturing, how to control the direction of fracture propagation, and how to apply the fluid load to simulate the continuum injection. Previously, some hydraulic fracturing models have mitigated these issues.[21−23]

In the present paper, based on the theory of the fluid flow of seepage porous media and damage mechanics, an anisotropic tensor format is established for the hydromechanical properties of porous media; a poromechanical model of hydraulic fracture propagation is proposed, and the FEM numerical weak coupling calculation method of hydraulic fracturing is realized. This comprises several components: (1) the fracture opening is calculated based on damage localization, employing the thickness of localization; (2) the strain energy loss resulting from fracturing is compensated by the fluid pressure invasion through poroelastic coupling; (3) the direction of fracture propagation is controlled by the tensors of the hydro-mechanical properties induced by hydraulic fracture opening; and (4) continuous injection is achieved with the fracture growth through a loading scheme of stepwise increases in solution duration. As an example, the model is used to assess hydraulic fracture propagation in a three-layer reservoir; the morphology of the fracture zone and parameters such as length, width, and fluid pressure are validated with the analytical solutions. The model exhibits four stages of fracture propagation: fracture nucleation, kinetic propagation, steady propagation, and propagation termination, which represents the full coupling between the fracture tip and fluid front.

2. CONTROLLING EQUATIONS

We define the relationships that enable the simulation of the effects of fluid pressure on the propagation of a fluid-driven fracture. This involves both the transport of fluid and the mechanism of fracture expansion driven by that fluid.

2.1. Flow in Porous Media. Under the action of pressure gradient, water flow penetrates into the porous media of the coal reservoir, which is a dynamic process of hydraulic expansion. The porosity–elastic coupling conceptual model is shown in Figure 1. In the initial stage of dynamic adjustment, the q value of the velocity of fluid flowing into the pore is greater than that flowing out, and the redundant water accumulates in the pores to form pore fluid pressure P resulting in the effective stress σ' increasing. Second, with the increase of P, the inflow pressure gradient gradually decreases, while the outflow pressure gradient gradually increases. In the final stage, the pressure gradient at the inflow end and outflow end disappears, the q of the inflow is equal to the outflow, and the seepage of porous media reaches a steady-state flow.

During reservoir formation, the porous flow satisfies Darcy's law:[24]

$$q = K\nabla P \tag{1}$$

where ∇ is the differential operator vector and K is the permeability. Using the law of mass conservation, the pore pressure is determined as

$$\frac{d\xi}{dt} + \nabla^T q = \varpi \tag{2}$$

where ξ is the mass of fluid, ϖ is the fluid generation rate of a unit solid volume, and t is time. According to the coupling between the compressibility of the solid and fluid, the differential change in the fluid mass, $d\zeta$, can be represented as

$$d\zeta \equiv \frac{1}{V_b}\frac{dm}{\rho_f} = (\phi C_{pp}\, dP + \phi C_f\, dP) - \phi C_{pc}\, dP_c \tag{3}$$

where ρ_f is the mass density of the fluid, dm is the differential increment of fluid mass, V_b is the bulk volume, and ϕ is the porosity. Equation 3 shows that the volume increment of a fluid consists of three parts, where $\phi C_{cc}dP$ and $\phi C_f dP$ are the pore volume increments caused by the fluid pressure increment, dP, resulting from pore elasticity and fluid compressibility; $\phi C_{pc}dP_c$ is the compressive volume increment of the pore volume caused by an increment in the confining stress dP_c. The coefficient C_{pp} represents the internal expansibility in volume resulting from increments in the fluid pressure, C_{pc} is the internal contractility in volume resulting from increments in the confining stress, and C_f represents the fluid compressibility resulting from increments in the fluid pressure:[25]
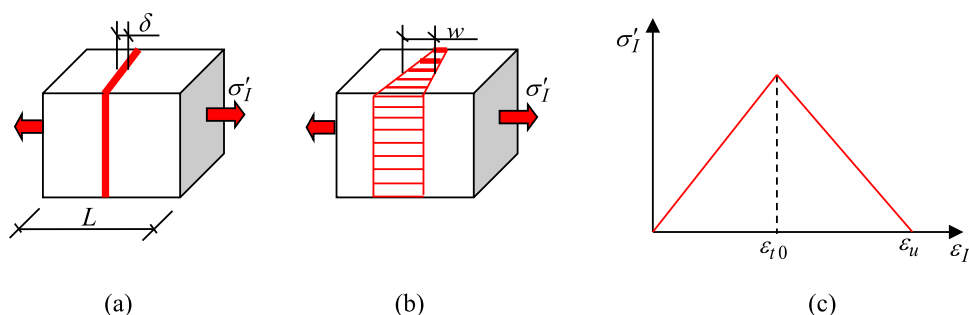
Figure 2. Cohesive zone model of hydraulic fracture: (a) the localized damaged band; (b) the cohesive breakdown process; and (c) the relationship between effective stress and strain.

$$C_{pp} = \frac{1}{V_p}\left(\frac{\partial V_p}{\partial P}\right)_{P_c}, \quad C_{pc} = -\frac{1}{V_p}\left(\frac{\partial V_p}{\partial P_c}\right)_{P}, \quad C_f = \frac{1}{\rho_f}\left(\frac{\partial \rho_f}{\partial P}\right)_{P_c} \tag{4}$$

where V_p is the pore volume and $P_c = \sigma_{ii}/3$ is the average stress, whose sign convention is defined as positive for compression. Further, we can define the storage coefficient of fluids by adding the first and third expressions in eq 4, as $C = C_{pp} + C_f$. Rewriting eq 3 and substituting this into eq 2 yield

$$\phi C \frac{dP}{dt} = \nabla^T(K\nabla P) + \varpi + \phi C_{pc}\frac{dP_c}{dt} \tag{5}$$

This states that in any element of the porous media, increments in the fluid volume comprise three parts: the net increment that flows in minus that flowing out, source generation, and drainage resulting from external stress increments, which correspond to the three terms in the right-hand side of this equation.

2.2. Stress Rebalancing. The pore fluid pressure will enlarge the longitudinal strains, such that the total strain is the superposition of the confining stress-induced strain and pore pressure-induced longitudinal strains, as follows:

$$\boldsymbol{\varepsilon} = \mathbf{E}^{-1}\boldsymbol{\sigma} + \beta\Delta P \tag{6}$$

where $\boldsymbol{\varepsilon}$ is the total strain vector, $\mathbf{E}$ is the stiffness matrix, $\boldsymbol{\sigma}$ is the (confining) stress vector, $\Delta P = P - P_0$ is an increment in the pore fluid pressure, P_0 is the reference pore fluid pressure, and β is the linear expansion coefficient vector resulting from internal forces of fluid pressure increments. In the initial state, β is isotropic—$\beta = \beta_x = \beta_y = \beta_z$—and is defined as

$$\beta = \frac{1}{3}C_{bp} \tag{7}$$

in which C_{bp} is the bulk expansion coefficient, defined as[25]

$$C_{bp} = \frac{1}{V_b}\left(\frac{\partial V_b}{\partial P}\right)_{P_c} \tag{8}$$

By employing the concept of thermal elasticity, β can also be calculated as

$$\beta = \frac{\alpha}{3K_d} \tag{9}$$

where K_d is the bulk modulus of the solid skeleton and α is the Biot coefficient; therefore the stresses corresponding to the total strains in eq 6 are the effective stress σ', which can be written as

$$\sigma' = \sigma + \alpha\Delta P \tag{10}$$

Since the pore fluid pressure is not uniformly distributed, the effective stress will lead to stress redistribution. The tensor form of the stress differential equation can be written as

$$\sigma_{i,j} + \alpha P_j + f_i = 0 \tag{11}$$

where f_i is the body force per unit volume.

3. FRACTURE OPENING AND ANISOTROPY

The key features to use FEM to represent hydraulic fracture propagation include the following: establishing the fracture opening in a continuum element and establishing a series of second-order Cartesian tensors regarding the damage, poroelasticity coefficients, and permeability.

3.1. Fracture Opening. Progressive fracturing in geomaterials is a multiscale phenomenon that can be divided into three main stages: the evolution of distributed microdamage, localization and subsequent macrocrack nucleation, and macrocrack propagation.[26−28] For FEM, the entire fracture process can be represented by a damage variable D as follows:

$$D = \begin{cases} 0, & \varepsilon_I < \varepsilon_{t0} \\ 1 - \kappa\left(\frac{\varepsilon_{tu}}{\varepsilon_I} - 1\right), & \varepsilon_{t0} \leq \varepsilon_I < \varepsilon_{tu} \\ 1, & \varepsilon_{tu} \leq \varepsilon_I \end{cases} \tag{12}$$

where ε_{t0} is the threshold strain, representing the initiation of crack nucleation; ε_{tu} is the final strain when the fracture has transected the porous element; κ is a combined parameter, calculated as $\kappa = \varepsilon_{t0}/(\varepsilon_{tu} - \varepsilon_{t0})$; and ε_I is the tensile strain controlling fracture opening. This tensile strain is in the same direction as the first effective principal stress σ_I' (Figure 2a,b), while the effective stress follows the cohesive law (Figure 2c).

The magnitude of fracture opening can be determined from the strain and damage by employing the thickness of the damage localization band, denoted as δ, and is typically 1−2 times the size of the cleat spacing. The element size is denoted as L. It can be divided into two zones in the tensile direction: a concentrated damage zone of dimension δ and an undamaged zone of dimension $L - \delta$. Both zones are subject to the same stress, σ'; therefore,

$$\frac{w}{\delta}(1 - D)E_0 = \frac{w^t - w}{L - \delta}E_0 = \sigma' \tag{13}$$

where w represents fracture opening, w^t represents the total elongation of the element, and E_0 represents the initial elastic modulus. From this equation, we have the following relation:

$$w^t = \frac{(1 - D)(L - \delta) + \delta}{\delta}w = \frac{(1 - D)L + D\delta}{\delta}w \quad (14)$$

The total strain can be expressed as

$$\varepsilon_I = \frac{w^t}{L} \quad (15)$$

Substituting eq 15 into eq 14 gives the hydraulic fracture opening:

$$w = \varepsilon_I \frac{\delta}{F\frac{\delta}{L} + (1 - D)} \quad (16)$$

According to eq 6, the relationship between strain and stress can be written as

$$\varepsilon_I = \frac{\sigma_1}{E_0} + \beta\Delta P \quad (17)$$

By substitution of eq 17 into eq 16, the constitutive relationship between fracture opening and fluid pressure is obtained as

$$w = \frac{\delta\left[\frac{\sigma_1}{E_0} + \beta\Delta P\right]}{F\frac{\delta}{L} + (1 - D)} \quad (18)$$

where σ_1 is the minimum confining stress normal to the fracture surfaces, taken as negative.

3.2. Fracture-Induced Anisotropy. The presence of a hydraulic fracture will lead to anisotropy in the hydro-mechanical properties, including the damage, coefficients of poroelasticity, and permeability. These may be represented using a series of second-order Cartesian tensors, which are defined in the global coordinates.[29,30]

3.2.1. Anisotropy of Damage. The damage tensor D_{ij} in global coordinates can be converted from D_{ij}^σ, which is defined in the coordinates of the principal stresses $(\sigma_1, \sigma_2, \sigma_3)$ as

$$D_{pq} = M_{pi}M_{qj}D_{ij}^\sigma \quad (19)$$

where M_{ij} is the conversion matrix, defined as

$$\mathbf{M} = [M_{ij}] = [e'_i \times e_j] \quad (20)$$

and the D_{ij}^σ are given by

$$D_{11}^\sigma = D_n, \quad D_{ij}^\sigma = 0 \; (i, j \neq 1) \quad (21)$$

where D_n represents the tensile damage in the direction of σ_1, which is derived from eq 14. Therefore, the damage tensor in global coordinates is written as

$$D_{pq} = M_{p1}M_{q1}D_n \quad (22)$$

3.2.2. Anisotropy of Poroelasticity Coefficients. A hydraulic fracture also leads to anisotropy in the coefficients C_{pp} and C_{bp}. Therefore, a set of damage correlation coefficients are introduced to realize anisotropy, as follows:

$$C_{pp} = C_{pp}\psi, \quad C_{bp} = C_{bp}\Sigma \quad (23)$$

where ψ and Σ are the orthotropic coefficient vectors, with the components taking the following forms:

$$\psi_i = \frac{1}{1 - D_i}, \quad \Sigma_i = \frac{1}{1 - D_i} \quad (i = 1, 2, 3) \quad (24)$$

where D_i represents damage in the global directions of x, y, and z.

3.2.3. Anisotropy of Permeability. The permeability tensor resulting from a series of joint sets or fractures is well understood.[31,32] However, these only consider fluid flow along the fracture, neglecting the normal flow, which represents the leak-off. We established a permeability tensor considering both flows, as follows

$$\mathbf{K} = \mathbf{M}^T\mathbf{K}^\sigma\mathbf{M} \quad (25)$$

where $\mathbf{K}$ and $\mathbf{K}^\sigma$ are the matrices of the permeability coefficients in global coordinates and principal stress coordinates, respectively, and $\mathbf{K}^\sigma$ is written as

$$\mathbf{K}^\sigma = \frac{1}{\mu}\begin{bmatrix} (k_n - k_l)N_1N_1 + k_l & (k_n - k_l)N_1N_2 & (k_n - k_l)N_1N_3 \\ (k_n - k_l)N_2N_1 & (k_n - k_l)N_2N_2 + k_l & (k_n - k_l)N_2N_3 \\ (k_n - k_l)N_3N_1 & (k_n - k_l)N_3N_2 & (k_n - k_l)N_3N_3 + k_l \end{bmatrix} \quad (26)$$

where N_1, N_2, and N_3 are the three projections of the normal vector N of fracture surfaces on the three principal stress vectors; and k_n and k_l are the normal and tangent permeabilities, respectively.

The normal permeability k_n can be obtained by multiplying the in situ permeability k by a modification ξ as follows:

$$k_n = k\xi \quad (27)$$

The in situ permeability decreases exponentially as the effective stress increases[25] and is calculated as follows:

$$k = k_0 e^{-(\zeta\sigma_m'/\sigma_0)} \quad (28)$$

where k_0 is the intrinsic permeability tested in the lab; σ_m' is the effective average stress, noted as compression positive; σ_0 is the reference stress, evaluated as the mean, maximum, or minimum of the magnitude vector of σ_m'; and ζ is a constant that ranges between 1.0 and 1.6.

The permeability along the fracture k_l follows a cubic law[33,34] as follows:

$$k_l = \frac{w^3}{12} \quad (29)$$

In this section, all of the components necessary for the simulation of hydraulic fracture propagation are established. In the next section, these factors are formulated into weakly coupled FEM equations, which work through the coupling analysis scheme.

4. COUPLING ANALYSIS

4.1. FEM Format of Coupling Equations. The differential equations eqs 5 and 11 can be transformed into FEM formats by utilizing the Galerkin variational principle; in the solid solution domain, the FEM format of eq 11 is written as

$$\mathbf{K}_s\mathbf{a} = \mathbf{P}_s + \mathbf{P}_f \quad (30)$$

where $\mathbf{K}_s$ is the global stiffness matrix, $\mathbf{a}$ is the column matrix of the unknown nodal displacements, $\mathbf{P}_s$ is the column matrix of solid load, and $\mathbf{P}_f$ is the column matrix of fluid pressure, calculated as

$$\mathbf{P}_f = \sum_e \int_{\Omega_e} \mathbf{B}^T \mathbf{E} \varepsilon_f d\Omega = \sum_e \int_{\Omega_e} \mathbf{B}^T \mathbf{E} \beta \Delta P d\Omega \qquad (31)$$

where $\mathbf{E}$ is the elasticity stiffness matrix of the porous rock, $\mathbf{B}$ is the element strain matrix, and ε_f is the column matrix of incremental strain generated by the incremental pore pressure ΔP.

In the fluid solution domain, the FEM format of eq 6 can be written as

$$\mathbf{C}\dot{\mathbf{P}} + K_f \mathbf{P} = \mathbf{Q} \qquad (32)$$

where $\mathbf{P}$ is the column matrix of the unknown pore pressure, $\dot{\mathbf{P}} = d\mathbf{P}/dt$; K_f is the permeability matrix; $\mathbf{C}$ is the matrix of storage coefficients; and $\mathbf{Q}$ is the column matrix of the flow rate. The latter two can be calculated as follows:

$$\mathbf{C} = f(\mathbf{C}_{pp} + \mathbf{C}_f) \qquad (33)$$

and

$$\mathbf{Q} = \mathbf{Q}_q + \mathbf{Q}_g + \mathbf{Q}_{P_c} \qquad (34)$$

where $\mathbf{C}_{pp}$ and $\mathbf{C}_f$ are the matrices of poroelasticity assembled using the coefficients defined in eq 5 and $\mathbf{Q}_q$, $\mathbf{Q}_g$, and $\mathbf{Q}_{pc}$ are the column matrices of the flow rate, generation rate, and confining stress change-induced fluid content change, respectively. All of the global matrices are assembled as

$$K_f = \sum_e \mathbf{K}^e, \quad \mathbf{C} = \sum_e \mathbf{C}^e, \quad \mathbf{Q} = \sum_e \mathbf{Q}^e \qquad (35)$$

in which

$$\begin{cases} \mathbf{K}^e = \int_{\Omega^e} B^T K B \, d\Omega \\ \mathbf{C}^e = f(C_{pp} + C_f) \int_{\Omega^e} N N^T \, d\Omega \end{cases} \qquad (36)$$

and

$$Q_g^e = \varpi \int_{\Omega^e} N \, d\Omega$$

$$Q_g^e = \varpi \int_{\Omega^e} N \, d\Omega$$

$$Q_{P_c}^e = \varphi C_{pc} \frac{dP_c}{dt} \int_{\Omega^e} N \, d\Omega \qquad (37)$$

where N is the shape function matrix. The weak coupling format of eqs 32 and 34 is written as

$$\begin{bmatrix} 0 & 0 \\ 0 & C \end{bmatrix} \begin{Bmatrix} \dot{a} \\ \dot{P} \end{Bmatrix} + \begin{bmatrix} K_s & 0 \\ 0 & C \end{bmatrix} \begin{Bmatrix} a \\ P \end{Bmatrix} = \begin{Bmatrix} P_s + P_f \\ Q \end{Bmatrix} \qquad (38)$$

4.2. Analysis Process. As shown in the analysis flow chart in Figure 3, the coupling analysis can be divided into several calculation steps:

(1) Establish the in situ stress and permeability fields. The in situ stress distribution determines the permeability distribution around the injection hole, which—in turn—determines the initial location of fracture propagation.

(2) Porous flow analysis, where transient analysis is carried out with the fluid flux as the surface load, permeability as the input, and pore pressure as the output.
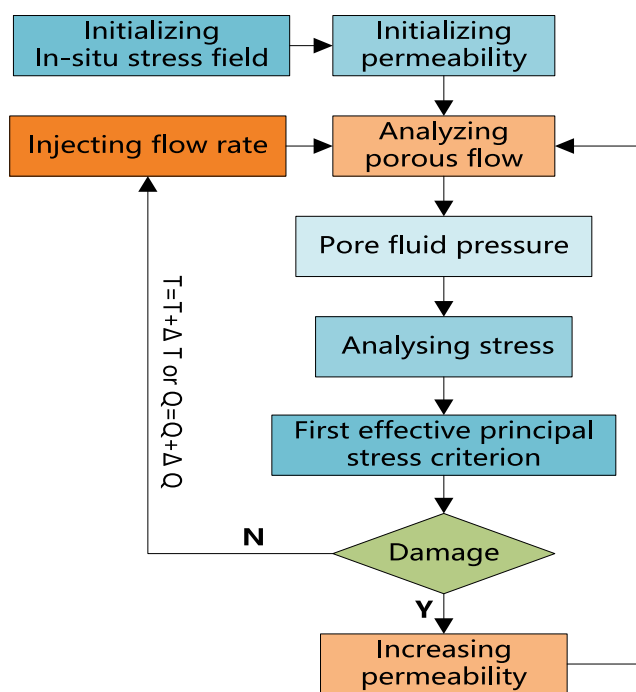

Figure 3. Flow diagram of the coupling analysis.

(3) Stress adjustment analysis, where the pore fluid pressure is input as the body force, and the strains and effective stresses are attained through static solutions.

(4) Damage judgment: if no new damaged elements are generated, the injection flow rate or injection time must be increased, and the abovementioned processes must be repeated; else, the fracture opening and anisotropy of hydromechanical properties are calculated, and the input parameters are renewed.

(5) The above steps can be repeated to realize a numerical simulation of the complex hydraulic fracture propagation.

4.3. Fluid Loading Scheme. To identify fracture growth during continuous injection, a loading scheme that gradually increases the duration of the solution is employed. This requires the assumption that the fracture is completely closed when the hydraulic fluid is drained, such that the parameters of the hydromechanical properties can be elastically handled. As shown in Figure 4a, C_V represents the global elasticity rigidness of the surrounding rock, which decreases with the fracture propagation, while the increasing fluid loading is carried out by the increasing injection volume V. Based on this, the loading scheme is shown in Figure 4b, where in each transient seepage field calculation, the volume of the injected fluid $QT^{(n)}$ is applied in full form in the rock fracturing circle. The transient calculation time length of each step is expressed in eq 41, such that the gradual expansion of the transient seepage field can be achieved by continuously increasing the number of cyclic steps. Further, to simulate an actual injection process, a limit flow rate Q_m and a character time up to this pressure T_0 are set up as follows:

$$Q^{(n)} = \begin{cases} \dfrac{Q_m}{T_0} T^{(n)}, & T^{(n)} < T_0 \\ Q_m, & T_0 \leq T^{(n)} \end{cases} \qquad (39)$$
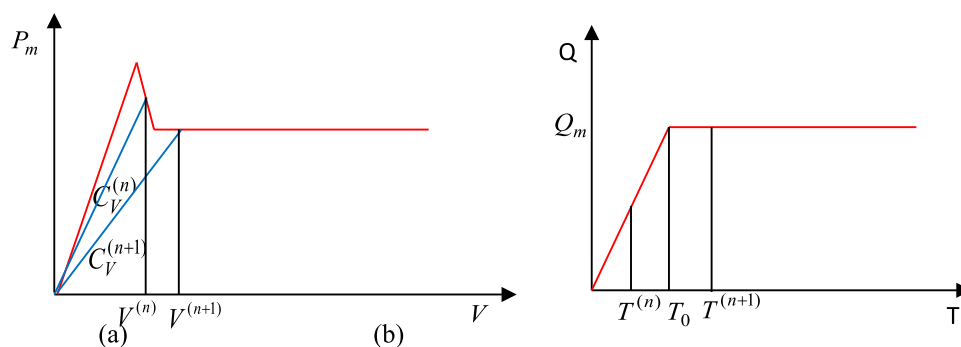
Figure 4. Loading scheme at the full flow rate: (a) relationship of fluid pressure at the crack mouth and loading flow rate; and (b) loading divisions of the flow rate.
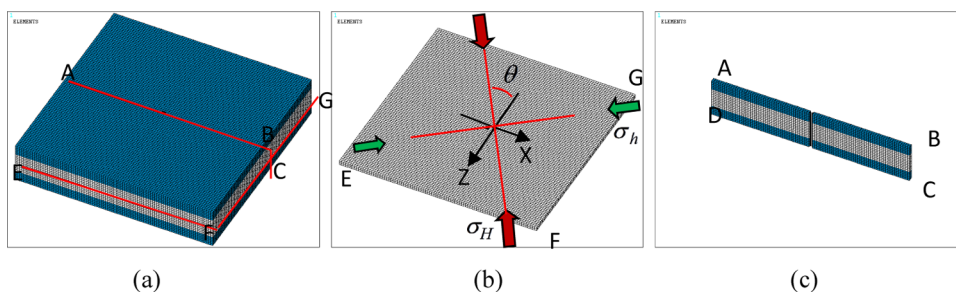
Figure 5. (a) Three-dimensional (3-D) FEM model, (b) the horizontal middle section, and (c) the vertical middle section.

where $T^{(n)}$ represents the length at step n.

Correspondingly, the flux loaded on the walls of the injection hole through the coal bed is written as

$$q_0 = Q_{\mathrm{m}}/(\pi d h) \tag{40}$$

where h represents the coal bed thickness and d is the hole diameter. In this paper, $Q_{\mathrm{m}} = 10 \ \mathrm{m^3/min}$.

5. RESULTS AND DISCUSSION

5.1. FEM Model. The example model (Figure 5) is taken from a coal bed methane formation, which is buried at a depth of 750 m, has horizontal dimensions of 200 m × 200 m, has top and bottom bed thicknesses of 5 m, a coal bed thickness of $h = 10$ m, and an injection hole diameter of $d = 20$ mm. The minor horizontal principal stress is $\sigma_{\mathrm{h}} = 7.8$ MPa, the major horizontal principal stress is $\sigma_{\mathrm{H}} = \lambda\sigma_{\mathrm{h}} = 15.6$ MPa, and the stress ratio is $\lambda = 2.0$. The vertical stress is calculated as $\sigma_{\mathrm{v}} = \rho g H$, where ρ is the mass density of overlaying rocks, H is the buried depth, and g is the gravitational acceleration. All boundary displacements are set to zero since it is the requirement of implanting the initial stresses; on the other hand, it is more reasonable to reflect the real in situ deformation state. Figure 5a shows the formation compositions and positions of cross sections; Figure 5b,c shows the middle horizontal and vertical sections with the injection hole crossed, respectively. The direction of the horizontal major principal stress σ_{H} is expressed using angle θ, which rotates anticlockwise from the negative Z coordinate.

5.2. Properties of Porous Formation and Hydraulic Fluid. The formation parameters include the permeability, coefficients of poroelasticity, and damage model parameters. These are usually assumed to satisfy the Weibull distribution, with the probability density function as follows:

$$f(\Omega) = \frac{m}{\Omega}\left(\frac{\Omega}{\Omega_0}\right)^{m-1} \exp\left[-\left(\frac{\Omega}{\Omega_0}\right)^m\right] \tag{41}$$

where Ω represents the element property parameters, Ω_0 is the reference modulus, and m is the shape factor, which represents the homogeneity of the parameter distribution. The higher the m value, the better the homogeneity; in this paper, $m = 10$. The reference moduli are listed in Table 1, which reflects their average values. The hydraulic fluid properties are listed in Table 2.

5.3. Validation and Discussion of Results. *5.3.1. Hydraulic Fracture Zones.* The numerical results of the hydraulic fracture zone are shown in Figures 6−8, from which the basic features can be derived.

Table 1. Properties of Porous Formations

parameter	coal bed	top/bottom bed
intrinsic permeability, k_0 (mD)	1.462	0.146
porosity, ϕ	0.06	0.02
internal expansion coefficient, C_{pp} (MPa^{-1})	0.01	0.01
internal contraction coefficient, C_{pc} (MPa^{-1})	0.01	0.01
Biot coefficient, α	0.33	0.33
mass density, ρ (kg/m^3)	1200	2500
solid skeleton elasticity modulus, E_{d} (GPa)	9	11.56
solid matrix elasticity modulus, E_{s} (GPa)	13.42	15
Poisson's ratio, v	0.3	0.3
solid skeleton compression strength limit, σ_{c} (MPa)	7.7	16.25
ratio of compression to tension strength, γ	15	15
tensile strain threshold, $\varepsilon_{\mathrm{t0}}$, 10^{-3}	0.0085	0.015
final tensile strain, $\varepsilon_{\mathrm{tu}}$, 10^{-3}	0.085	0.65
thickness of localized damage band, δ (mm)	19	5

Table 2. Hydraulic Fluid Parameters

mass density, ρ_w (kg/m^3)	1000
compressibility coefficient, C_f (MPa^{-1})	4.5×10^{-4}
viscosity coefficient, μ (Pa·s)	1.005×10^{-3}

(1) Hydraulic fractures always propagate in the direction of the major principal stress σ_H, with the fracture surface normal to the minimum principal stress σ_h (Figure 6). This conforms to conventional knowledge, proving that the tensors established for the hydromechanical properties are correct and can effectively control the direction of fracture propagation.[8,11,21,22]

(2) Figure 6 shows that the horizontal cross section of the fracture zone and fluid pressure contours can be approximated as ellipses. This is consistent with the results found by Liu.[35]

(3) The vertical section also approximates an ellipse, which is slightly cut through the top and bottom beds in the vicinity of the injection hole (Figure 7c). This conforms to the results found by Peirce[36] for three-layered formations.

5.3.2. Temporal Variation of Hydraulic Fracture Parameters. The parameters of hydraulic fractures include the fracture length, opening pressure, and fluid pressure. The fracture lengths are measured from the resultant pictures shown in Figure 8. The fracture opening and fluid pressure at the fracture mouth are measured by setting a monitor element at the fracture mouth during transient analysis. The comparisons of the temporal variations of these parameters via the analytical solutions are shown in Figures 910−11. The analytical solutions proposed by Nordgren[2] and Geertsman and Klerk[37] for KGD and PKN models in cases of high leak-off values are adopted herein:

$$L(t) = \frac{q_0}{\pi h C_1} t^{1/2}$$

$$w(0, t) = 4\left[\frac{2(1-v)\mu q_0^2}{\pi^3 GhC_1}\right]^{1/4} t^{1/8}$$

$$P(0, t) = 1.135\eta\left(\frac{Gq_0\mu}{(1-v)^3 L(t)^2}\right)^{1/4} + S \tag{42}$$

where G is the coal bed shear constant; S is the principal stress normal to fracture surfaces, $S = \sigma_h = 7.8$ MPa; η represents the effects of leak-off, $\eta = 0.32 \times 10^{-15}$; and C_1 is the leak-off coefficient involved with the permeability, porosity, in situ stresses, fracture toughness, and fluid viscosity, etc. It is valued[38] at $C_1 = 4.98 \times 10^{-4}$, and q_0 is the injection flow.

The comparisons show that the numeric solutions conform well with the analytical solutions, while some slight differences indicate that the numerical solutions can exhibit more plentiful information about hydraulic fracture propagation. Based on the porosity−elastic coupling model (Figure 1), combined with the damage−fracture evolution characteristics of materials, the process of hydraulic fracturing can be divided into four stages (Figure 11), which are conceptualized in Figure 12.

Stage-I: fracture nucleation, during which a macroembryo fracture takes form in the close vicinity of the injection hole. Since it is aggregated from distributive cracks, their gaps and bridging constitute fracture cohesive zones. In this stage, the peak fluid pressure is used to both overcome the traction of the cohesive zone and support the confining normal stress.

Stage-II: kinetic propagation, during which the sudden breaking of cohesive traction causes the fluid pressure at the fracture mouth to drop significantly, and the fracture opening increases quickly to a peak value, along with the fracture length.

Stage-III: steady propagation, during which the fluid pressure at the fracture mouth remains constant, while the fracture length increases quickly and the fracture opening slowly becomes constant.

Stage-IV: propagation termination, where—as the fracture length increases—the injection flow rate cannot increase due to leak-off, which gives rise to a slow drop in the fluid pressure, decreasing the fracture opening and propagation termination.

It is obvious that the analytical solutions ignore stage-I and stage-IV.

5.3.3. Spatial Variation of the Parameters of the Hydraulic Fracture. The analytical solutions of fracture opening and fluid pressure along the fracture length are referred to as the SCR asymptotes by Adachi and Detournay et al.:[39−41]

$$\left.\begin{array}{l} \Omega(\xi, \tau) = A(\tau)(1 - \xi)^\alpha, \, 0 < \alpha < 1 \\[2mm] \prod(\xi, \tau) = \frac{1}{4\gamma}A(\tau)\alpha \cot \pi\alpha(1 - \xi)^{\alpha-1} \\[2mm] \alpha = 2/3, \, A(\tau) = 2^{1/3}3^{5/6}(g_m\gamma^2\gamma')^{1/3} \end{array}\right\} \tag{43}$$

where Ω, Π, ξ, γ, τ, and g_m are the dimensionless forms of fracture opening, fluid pressure, position coordinate, fracture length, injection time, and viscosity scaling, respectively. The comparisons between the numerical solutions and the analytical solutions for fluid pressure and the half-width along the fracture length are shown in Figures 13 and 14. The contrast between the fluid pressure and half-width along fracture length is shown in Figure 15.

The comparison in Figure 13 shows that the fluid pressure of the numerical solution is distributed throughout the fracture
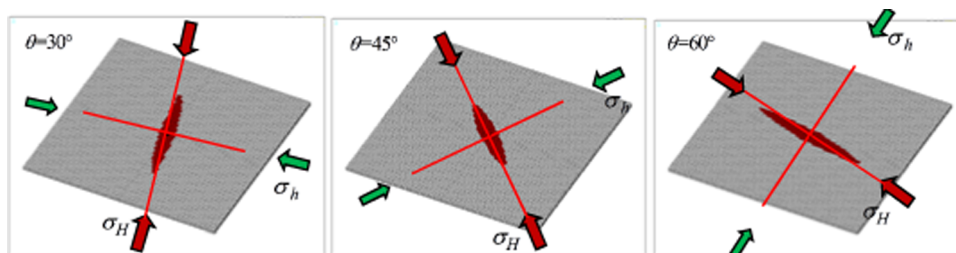
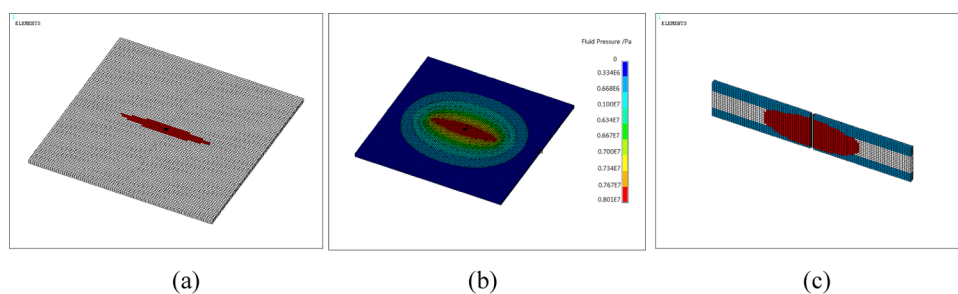**Figure 6.** Hydraulic fracture propagation in the direction of maximum principal stress.

Figure 7. (a) Horizontal middle section, (b) fluid pressure distribution, and (c) vertical middle section.
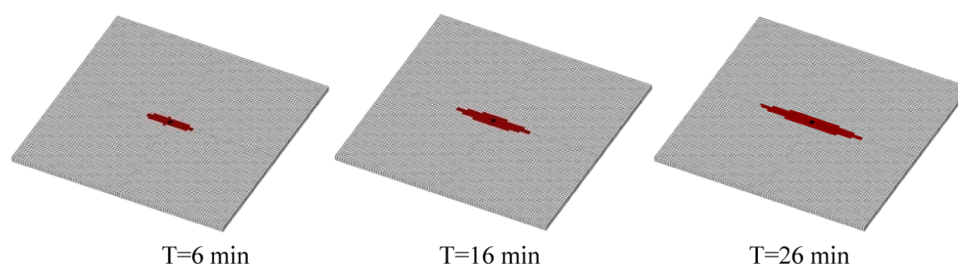

T=6 min   T=16 min   T=26 min

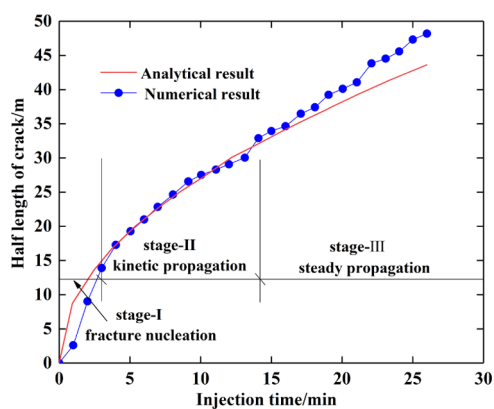**Figure 8.** Fracture length at different injection times.

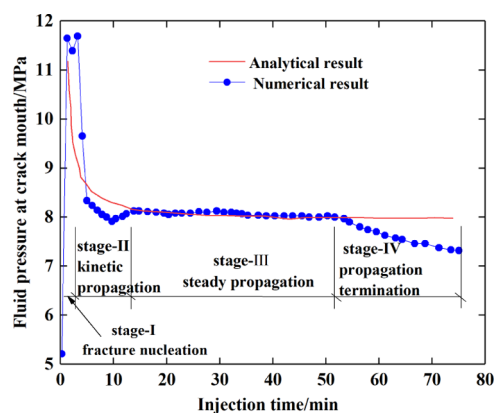
Figure 9. Half-length of the crack.

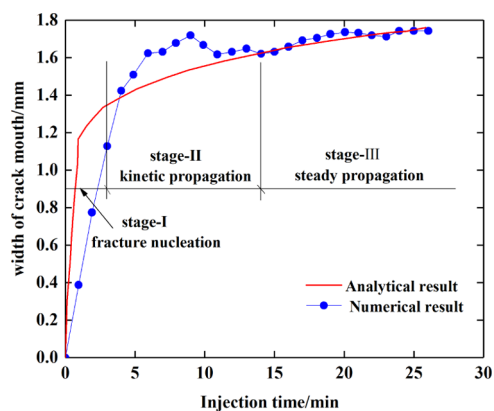**Figure 11.** Fluid pressure at the fracture mouth.

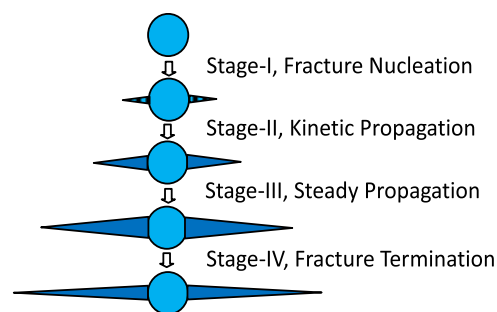**Figure 10.** Width of the crack at the fracture mouth.

**Figure 12.** Four-stage conceptual model.

and extends to the fracture tip. However, if we realize the premise of analytical solutions, the numerical solution is acceptable. Owing to mathematical difficulties, the coupling between the fracture tip and fluid front in analytical solutions is generally assumed to be progressive, such that the fluid pressure distribution always lags behind the fracture tip,

leading to the existence of a pressure void ahead of the fluid front. Therefore, we can regard the analytical solution as a case of incomplete coupling between the fracture tip and fluid front, which always occurs in situations with a large toughness, high viscosity, and no leak-off; in most cases, the fluid pressure distribution goes ahead of the fracture tip; complete coupling occurs, which is what the numerical solution represents. The comparisons in Figures 14 and 15 further indicate that there is a cohesive zone ahead of the fracture tip.
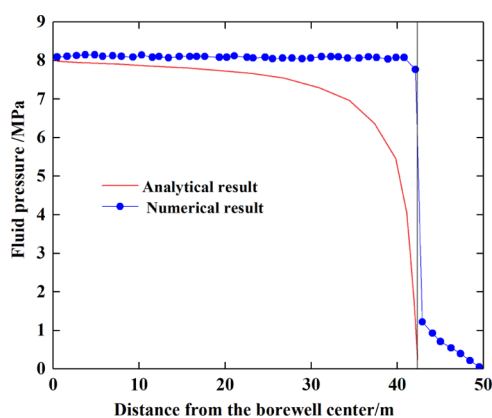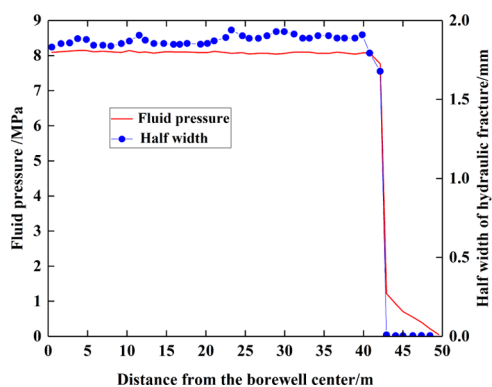
Figure 13. Comparison of numerical and analytical results of the fluid pressure.
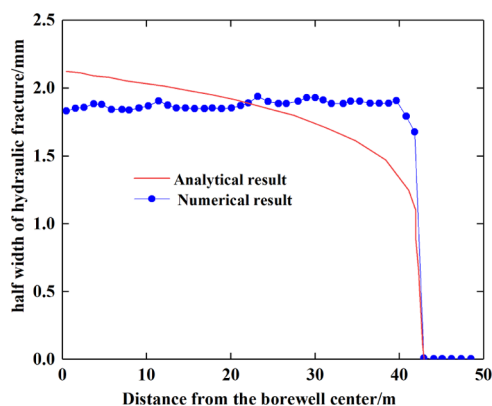

Figure 14. Comparison of numerical and analytical results of the half-width.

Figure 15. Numerical results of half-width and fluid pressure along the fracture length.

Based on these facts, two types of coupling modes in the fracture tip are proposed: the incomplete coupling model (Figure 16a) and complete coupling model (Figure 16b), which correspond to the analytical models and numerical solutions in the present paper, respectively. In the complete coupling model, $D = 1$ represents the completely fractured zone, $D = 0$ represents the elastically expanding zone of pore pressure; in between them, $1 > D > 0$ represents the cohesive fracture zone, where the fracture opening acts more like an aequilate "bag", indicating that the fluid pressure energy is mainly used to overcome in situ stress clamping and viscosity dissipation from the fluid front invasion and leak-off.
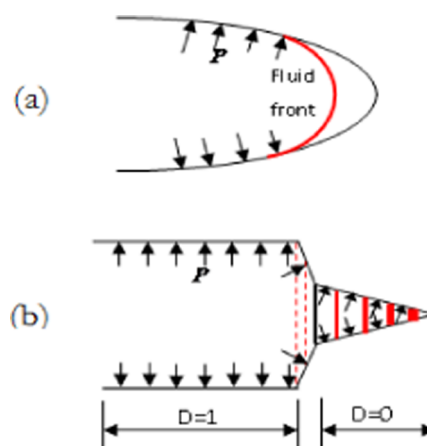
Figure 16. Two types of coupling models: (a) analytical model and (b) numerical model.

6. SUMMARY

In this paper, a numerical simulation of three-dimensional hydraulic fracturing is performed. The advantages of poromechanical modeling are as follows:

(1) It can reflect the temporal and spatial evolution and distribution of the stress field, damage field, and pore fluid pressure field around the injection hole during the process of hydraulic fracturing.

(2) Compared with the analytical solution, the numerical solutions of the fracturing parameters, including the fracture length, opening pressure, and fluid pressure, are more accurate. In particular, the reflection of the fluid pressure advance distribution at the crack tip and cohesive fracture is an improvement to the theoretical model.

(3) The established anisotropic tensor format for the hydromechanical properties of porous media can be used to simulate hydraulic fracturing in complex stress and inclined formation.

However, some further studies should be conducted on the following aspects:

(1) The thickness of the localized fracture band δ is a material parameter that should be specifically researched.

(2) The precision of the fracture zone is determined by element size, so proper selection of the RVE size should be studied.

■ AUTHOR INFORMATION

Corresponding Author

  Li Wang − *School of Civil Engineering, Henan Polytechnic University, Jiaozuo 454000, China;* ⓘ orcid.org/0000-0002-1085-7695; Email: wlcjwh@163.com

Authors

  Xinsheng Zhang − *Institute of Resources & Environment, Henan Polytechnic University, Jiaozuo 454000, China*

  Yunxing Cao − *Institute of Resources & Environment, Henan Polytechnic University, Jiaozuo 454000, China; Collaborative Innovation Center of Coalbed Methane and Shale Gas for Central Plains Economic Region, Henan Polytechnic University, Jiaozuo 454000, China*

Guo Xiaohui − *School of Civil Engineering, Henan Polytechnic University, Jiaozuo 454000, China*

■ ACKNOWLEDGMENTS

■ REFERENCES

(1) Geertsma, J.; De Klerk, F. A Rapid Method of Predicting Width and Extent of Hydraulically Induced Fractures. *J. Pet. Technol.* **1969**, *21*, 1571−1581.

(2) Nordgren, R. P. Propagation of a Vertical Hydraulic Fracture. *Soc. Pet. Eng. J.* **1972**, *12*, 306−314.

(3) Perkins, T. K.; Kern, L. R. Widths of Hydraulic Fractures. *J. Pet. Technol.* **1961**, *13*, 937−949.

(4) Settari, A.; Cleary, M. Development and Testing of a Pseudo-Three-Dimensional Model of Hydraulic Fracture Geometry. In *Proceedings of the 6th SPE Symposium on Reservoir Simulation*; Society of Petroleum Engineers, 1982; pp 185−214.

(5) Morales, R. H. Microcomputer Analysis of Hydraulic Fracture Behavior with a Pseudo-Three-Dimensional Simulator. *SPE Prod. Eng.* **1989**, *4*, 69−74.

(6) Barree, R. A Practical Numerical Simulator for Three-Dimensional Fracture Propagation in Heterogeneous Media. In *SPE Reservoir Simulation Symposium*, 1983; pp 403−413.

(7) Clifton, R. J.; Abou-Sayed, A. S. On the computation of the three-dimensional geometry of Hydraulic fractures. *SPE J.* **1979**, 7943.

(8) Wang, H.; Liu, H.; Zhang, J. Numerical simulation of hydraulic fracture height control with different parameters. *J. Univ. Sci. Technol. China* **2011**, *41*, 820−825.

(9) Biao, F. J.; Liu, H.; Zhang, S. C. A numerical study of parameter influences on horizontal hydraulic fracture. *Eng. Mech.* **2011**, *28*, 228−235.

(10) Zhang, G. M.; Liu, H.; Zhang, J. Simulation of hydraulic fracturing of oil well based on fluid-solid coupling equation and non-linear finite element. *Acta Pet. Sin.* **2009**, *30*, 113−116.

(11) Chen, Z.; Bunger, A. P.; Zhang, X.; Robert, G. J. Cohesive zone finite element-based modeling of hydraulic fractures. *Acta Mech. Solida Sin.* **2009**, *22*, 443−452.

(12) Rahman, M. M.; Rahman, M. K.; Rahman, S. S. Multicriteria Hydraulic Fracturing Optimization for Reservoir Stimulation. *Pet. Sci. Technol.* **2003**, *21*, 1721−1758.

(13) Tian, L.; Cao, Y.; Chai, X.; Liu, T.; Feng, P.; Feng, H.; Zhou, D.; Shi, B.; Oestreich, R.; Rodvelt, G. Best practices for the determination of low-pressure/permeability coalbed methane reservoirs, Yuwu Coal Mine, Luan mining area, China. *Fuel* **2015**, *160*, 100−107.

(14) Zhao, Q.; Lisjak, A.; Mahabadi, O.; Liu, Q.; Grasselli, G. Numerical simulation of hydraulic fracturing and associated microseismicity using finite-discrete element method. *J. Rock Mech. Geotech. Eng.* **2014**, *6*, 574−581.

(15) Zhang, F.; Damjanac, B.; Maxwell, S. Investigating Hydraulic Fracturing Complexity in Naturally Fractured Rock Masses Using Fully Coupled Multiscale Numerical Modeling. *Rock Mech. Rock Eng.* **2019**, *52*, 5137−5160.

(16) Fu, P.; Johnson, S. M.; Carrigan, C. R. An explicitly coupled hydro-geomechanical model for simulating hydraulic fracturing in arbitrary discrete fracture networks. *Int. J. Numer. Anal. Methods Geomech.* **2013**, *37*, 2278−2300.

(17) Ma, G.; Wang, Y.; Li, T.; Chen, Y. A mesh mapping method for simulating stress-dependent permeability of three-dimensional discrete fracture networks in rocks. *Comput. Geotech.* **2019**, *108*, 95−106.

(18) Zhao, K.; Stead, D.; Kang, H.; Damjanac, B.; Donati, D.; Gao, F. Investigating the interaction of hydraulic fracture with pre-existing joints based on lattice spring modeling. *Comput. Geotech.* **2020**, *122*, No. 103534.

(19) Grassl, P.; Fahy, C.; Gallipoli, D.; Wheeler, S. J. On a 2D hydro-mechanical lattice approach for modelling hydraulic fracture. *J. Mech. Phys. Solids* **2015**, *75*, 104−118.

(20) Wang, L.; Zhang, X.; Cao, Y. X.; TIian, L. Numeric simulation of plane strain hydraulic fracturing under multi-oriented perforations. *J. Henan Polytech. Univ.* **2018**, *37*, 124−132.

(21) Yang, T.; Tang, C.; Liang, Z. Brittleness damage of rock failure process and seepage coupling numerical model study. *Acta Mech. Sin.* **2003**, *35*, 533−541.

(22) Li, L.; Liang, Z.; Li, G. There-dimensional numerical analysis of traversing and twisted fractures in hydraulic fracturing. *Chin. J. Rock Mech. Eng.* **2010**, *29*, 3208−3215.

(23) Lu, Y. L.; Derek, E.; G, W. L. Microcrack-based coupled damage and flow modeling of fracturing evolution in permeability brittle rocks. *Comput. Geotech.* **2013**, *49*, 226−244.

(24) Kong, X. Y. *Advanced Poromechanics*; Press of University of Science and Technology of China: Hefei, China, 2000.

(25) Zimmerman, R. W. Coupling in poroelasticity and thermo-elasticity. *Int. J. Rock Mech. Min. Sci.* **2000**, *37*, 79−87.

(26) Bažant, Z. P.; Bažant, H. O. Crack band theory for fracture of concrete. *Mater. Constr.* **1983**, *16*, 155−177.

(27) Wang, L.; Ye, J.; Mao, Y.; Yang, J.; Rui, D. Microcracks size growth prediction based on microdefects nucleation number. *Int. J. Fract.* **2013**, *182*, 239−249.

(28) Wang, L.; Mao, Y. C.; Ye, J. S. Models for microcracks extension and damage evolution based on number series of microdefects nucleation. *Eng. Mech.* **2013**, *30*, 278−286.

(29) Wangen, M. A 3D model of hydraulic fracturing and microseismicity in anisotropic stress fields. *Geomech. Geophys. Geo-Energy Geo-Resour.* **2019**, *5*, 17−35.

(30) Rong, G.; Peng, J.; Wang, X.; Liu, G.; Hou, D. Permeability tensor and representative elementary volume of fractured rock masses. *Hydrogeol. J.* **2013**, *21*, 1655−1671.

(31) Oda, M.; Takemura, T.; Aoki, T. Damage growth and permeability change in triaxial compression tests of Inada granite. *Mech. Mater.* **2002**, *34*, 313−331.

(32) Zhou, C.; Xiong, W. Permeability tensor for jointed rock masses in coupled seepage and stress field. *Chin. J. Rock Mech. Eng.* **1996**, *15*, 338−344.

(33) Robert, W. Z.; Gudmundur, S. B. Hydraulic conductivity of rock fractures. *Transp. Porous Media* **1996**, *23*, 1−30.

(34) Witherspoon, P. A.; Wang, J. S. Y.; Iwai, K.; Gale, J. E. Validity of Cubic Law for fluid flow in a deformable rock fracture. *Water Resour. Res.* **1980**, *16*, 1016−1024.

(35) Liu, Z.; Wang, T.; Gao, Y. The key mechanics problems on hydraulic fracture in shale. *Chin. J. Solid Mech.* **2016**, *37*, 39−49.

(36) Peirce, A. Modeling multi-scale processes in hydraulic fracture propagation using the implicit level set algorithm. *Comput. Methods Appl. Mech. Eng.* **2015**, *283*, 881−908.

(37) Geertsma, J.; Haafkens, R. A Comparison of the Theories for Predicting Width and Extent of Vertical Hydraulically Induced Fractures. *J. Energy Resour. Technol.* **1979**, *101*, 8−19.

(38) Zeng, X. H.; Guo, D. L.; Wang, Z. W. Study on the calculating method of the total fracturing fluid leak-off coefficient. *J. Southwest Pet. Univ.* **2005**, *27*, 53−56.

(39) Peirce, A. A Hermite cubic collocation scheme for plane strain hydraulic fractures. *Comput. Methods Appl. Mech. Eng.* **2010**, *199*, 1949−1962.

(40) Adachi, J. I.; Emmanuel, D. Plane strain propagation of a hydraulic fracture in a permeable rock. *Eng. Fract. Mech.* **2008**, *75*, 4666−4694.

(41) Desroches, J.; Detournay, E.; Lenoach, B. The Crack Tip Region in Hydraulic Fracturing. *Proc. R. Soc. London, Ser. A* **1994**, *447*, 39−48.